Numerical Solution of Biot Equations in Quasi-static State

Sergey Solovyev, Mikhail Novikov, Alena Kopylova, and Vadim Lisitsa(✉)

Sobolev Institute of Mathematics SB RAS, 4 Koptug ave., Novosibirsk 630090, Russia
{solovievsa,lisitsavv}@ipgg.sbras.ru

Abstract. This paper presents a numerical algorithm to simulate low-frequency loading of fluid-filled poroelastic materials and estimate the effective frequency-dependent strain-stress relations for such media. The algorithm solves Biot equation in quasi-static state in the frequency domain. Thus, a large-scale system of linear algebraic equations have to be solved for each temporal frequency. We use the direct solver, based on the *LU* decomposition to resolve the system of the linear equations. According to the presented numerical examples suggested algorithm allows reconstructing the stiffness tensor within a wide range of frequencies for the realistic large-scale samples within several minutes. Thus, the estimation of the frequency-dependent stiffness tensors can be done in a routine manner and statistical data may be accumulated.

Keywords: Biot equation · Poroelasticity · Finite differences

1 Introduction

Developments in CO_2 sequestration [8,14], geothermal energy exploration [12,21] technologies raises a challenging tasks to seismic monitoring methods (4D seismic). One needs to estimate the fluid mobility and reservoir hydraulic permeability based on seismic data. Standard seismic attributes, especially the kinematic ones, are almost incentive to the changes in the reservoir structure due to the fluid substitution or partial chemical dissolution of carbonate rock matrix. However, the frequency-dependent dynamic effects can be recorded and potentially interpreted. In particular, changes in the fluid content or the pore-space geometry significantly affects the wave-induced fluid flows (WIFF). These flows are caused by the local pressure gradients within the wavefront if a seismic wave propagates in fractured-porous media [16,19]. Typically, fracture-to-background WIFF (FB-WIFF) and fracture-fracture WIFF (FF-WIFF) are considered. The FB-WIFFs appear if a low-frequency (long wavelength) wave propagates. In this case, the wave period is high enough for flow to form, even in the media

The research was supported by the Russian Science foundation grant no. 19-77-20004.

© Springer Nature Switzerland AG 2021
O. Gervasi et al. (Eds.): ICCSA 2021, LNCS 12949, pp. 519–531, 2021.
https://doi.org/10.1007/978-3-030-86653-2_38

with quite low permeability. The intensity of FB-WIFF is governed by a compressibility contrast between the host rock and fracture-filling material [10,19]. High-frequency signals propagation causes FF-WIFF, defined by fracture-filling material properties and also local fracture connectivity [7,10,19]. Unfortunately, theoretical studies of this effect include consideration of relatively simple models of the media. Moreover, the fracture connectivity is considered only for the pairs of differently oriented fractures [10]. Numerical investigation of the phenomena is also restricted by such fracture connectivity criteria [10,19], except the study [9], where authors apply statistical modeling of fracture network and estimate resulting connectivity of the fractures. One of the reasons for that is the lack of efficient numerical algorithm to simulate seismic wave propagation in poroelastic media, or to solve Biot equation in quasi-static state to simulate low-frequency creeping test. Numerical upscaling experiments should satisfy two requirements. First, each considered sample should be representative [1,18], or, at least, should be much greater that the typical homogeneity size. In the case of the fractured-porous media, the characteristic size in the fracture length, typical percolation length, or connectivity index [17,25]. However, the grid step for either finite difference or finite element method is governed by the fracture width. Thus, the typical size of the discretized problem exceeds 1000 grid points in each spatial direction. Second, numerical upscaling requires a series of experiments for each statistically equivalent models of the fracture systems. Thus, an efficient numerical upscaling algorithm should be able to solve series on large-scale problems.

In this paper, we present an algorithm for numerical upscaling elastic properties of fractured-porous media in low-frequency range. To do so, we develop the algorithm to solve Biot equation in quasi-static state. The paper has the following structure. In Sect. 2, we state the problem of the poroelastic media upscaling to obtain frequency-dependent stiffness tensor, corresponding to the viscoelastic media. The finite-difference approximation of the considered boundary-value problem in considered in Sect. 3. Next, we provide the peculiarities of the numerical solution of the SLAE is provided in Sect. 4. Numerical experiments and performance analysis is presented in Sect. 5.

2 Statement of the Problem

2.1 Biot Equations in Quasistatic State

Consider the quasi-static Biot equations governing the diffusion processes in fluid-filled poroelastic media in a low-frequency regimes [2,3]. We deal with the Cartesian coordinates and restrict our considerations with 2D case, thus the equations can be written as follows:

$$\begin{gathered}
\frac{\partial}{\partial x}\left[(\lambda_u+2\mu)\frac{\partial u_x}{\partial x}+\lambda_u\frac{\partial u_z}{\partial z}+\alpha M\left(\frac{\partial w_x}{\partial x}+\frac{\partial w_z}{\partial z}\right)\right]+\frac{\partial}{\partial z}\left[\mu\left(\frac{\partial u_x}{\partial z}+\frac{\partial u_z}{\partial x}\right)\right]=0,\\
\frac{\partial}{\partial x}\left[\mu\left(\frac{\partial u_x}{\partial z}+\frac{\partial u_z}{\partial x}\right)\right]+\frac{\partial}{\partial z}\left[\lambda_u\frac{\partial u_x}{\partial x}+(\lambda_u+2\mu)\frac{\partial u_z}{\partial z}+\alpha M\left(\frac{\partial w_x}{\partial x}+\frac{\partial w_z}{\partial z}\right)\right]=0,\\
\frac{\partial}{\partial x}\left[\alpha M\left(\frac{\partial u_x}{\partial x}+\frac{\partial u_z}{\partial z}\right)+M\left(\frac{\partial w_x}{\partial x}+\frac{\partial w_z}{\partial z}\right)\right]=i\omega\frac{\eta}{k_0}w_x,\\
\frac{\partial}{\partial z}\left[\alpha M\left(\frac{\partial u_x}{\partial x}+\frac{\partial u_z}{\partial z}\right)+M\left(\frac{\partial w_x}{\partial x}+\frac{\partial w_z}{\partial z}\right)\right]=i\omega\frac{\eta}{k_0}w_z,
\end{gathered} \tag{1}$$

where $\vec{u}=(u_x,u_z)^T$ is the solid matrix velocity vector, $\vec{w}=(w_x,w_z)^T$ is the vector of the relative fluid velocity with respect to the matrix, λ_u is the Lame parameter of undrained rock, μ is the shear modulus, α is Biot-Willis parameter, M is the fluid storage coefficient, η is the fluid dynamic viscosity, κ is the absolute permeability of the rock, and ω is the temporal frequency. Specific parameters λ_u, M, and α are usually estimated from the bulk moduli of drained K_d, fluid K_u, and the solid matrix K_s [13]:

$$\begin{gathered}
\alpha=1-\frac{K_d}{K_s},\ \lambda_u=K_u-\frac{2}{3}\mu,\ M=BK_u/\alpha,\\
B=\frac{1/K_d-1/K_s}{1/K_d-1/K_s+\phi(1/K_f-1/K_s)},\ K_u=\frac{K_d}{1-B\alpha}.
\end{gathered}$$

2.2 Effective Visco-Elastic Media

We aim to construct the effective frequency-dependent linear elastic media (visco-elastic media) [5], so that for any stresses applied to a unit volume the average strains in the reconstructed viscoelstic and the original fluid-saturated poroelastic media should coincide. The quasi-static state of the viscoelastic wave equation is

$$\begin{gathered}
\frac{\partial}{\partial x}\left[C_{11}(\omega)\frac{\partial v_x}{\partial x}+C_{13}(\omega)\frac{\partial v_z}{\partial z}\right]+\frac{\partial}{\partial z}\left[C_{55}(\omega)(\frac{\partial v_x}{\partial z}+\frac{\partial v_z}{\partial x})\right]=0,\\
\frac{\partial}{\partial x}\left[C_{55}(\omega)(\frac{\partial v_x}{\partial z}+\frac{\partial v_z}{\partial x})\right]+\frac{\partial}{\partial z}\left[C_{13}(\omega)\frac{\partial v_x}{\partial x}+C_{33}(\omega)\frac{\partial v_z}{\partial z}\right]=0,
\end{gathered} \tag{2}$$

where $\vec{v}=(v_x,v_z)^2$ is the displacement vector, and tensor C is the frequency-dependent stiffness tensor. Consider a rectangular domain $D=[L_1^x,L_2^x]\times[L_1^z,L_2^z]$ with the following boundary conditions applied $\sigma\cdot\vec{n}=\sigma_0$ at ∂D, where $\vec{n}$ is the outer normal.

Consider three basis loads:

– x-direction compression:

$$\begin{gathered}
\sigma_{xx}=C_{11}(\omega)\frac{\partial v_x}{\partial x}+C_{13}(\omega)\frac{\partial v_z}{\partial z}|_{x=L_1^x}=\phi_x,\\
\sigma_{xx}=C_{11}(\omega)\frac{\partial v_x}{\partial x}+C_{13}(\omega)\frac{\partial v_z}{\partial z}|_{x=L_2^x}=\phi_x,\\
\sigma_{zz}=C_{13}(\omega)\frac{\partial v_x}{\partial x}+C_{11}(\omega)\frac{\partial v_z}{\partial z}|_{z=L_1^z}=0,\\
\sigma_{zz}=C_{13}(\omega)\frac{\partial v_x}{\partial x}+C_{11}(\omega)\frac{\partial v_z}{\partial z}|_{z=L_2^z}=0,\\
\sigma_{xz}=C_{55}(\omega)(\frac{\partial v_x}{\partial z}+\frac{\partial v_z}{\partial x})|_{\partial D}=0,
\end{gathered} \tag{3}$$

Solution of the problem (2), (3) can be constructed analytically, in case of constant coefficients: $\sigma_{xx}(x,z) = \phi_x$, $\sigma_{zz}(x,z) = 0$, and $\sigma_{xz}(x,z) = 0$. Thus the components of the strain tensor can be represented as

$$\begin{aligned} \varepsilon_{xx} &= \frac{\partial v_x}{\partial x} = S_{11}\phi_x, \\ \varepsilon_{zz} &= \frac{\partial v_z}{\partial z} = S_{13}\phi_x, \\ \varepsilon_{xz} &= \frac{1}{2}\left(\frac{\partial v_z}{\partial x} + \frac{\partial v_x}{\partial z}\right) = S_{15}\phi_x, \end{aligned} \tag{4}$$

where S_{ij} are the components of the compliance tensor (invert to stiffness tensor). If the initial loads are known and strains are computed, one may resolve the equations with respect to the components of the compliance tensor.

– z-direction compression:

$$\begin{aligned} \sigma_{xx} &= C_{11}(\omega)\frac{\partial v_x}{\partial x} + C_{13}(\omega)\frac{\partial v_z}{\partial z}|_{x=L_1^x} = 0, \\ \sigma_{xx} &= C_{11}(\omega)\frac{\partial v_x}{\partial x} + C_{13}(\omega)\frac{\partial v_z}{\partial z}|_{x=L_2^x} = 0, \\ \sigma_{zz} &= C_{13}(\omega)\frac{\partial v_x}{\partial x} + C_{11}(\omega)\frac{\partial v_z}{\partial z}|_{z=L_1^z} = \phi_z, \\ \sigma_{zz} &= C_{13}(\omega)\frac{\partial v_x}{\partial x} + C_{11}(\omega)\frac{\partial v_z}{\partial z}|_{z=L_2^z} = \phi_z, \\ \sigma_{xz} &= C_{55}(\omega)\left(\frac{\partial v_x}{\partial z} + \frac{\partial v_z}{\partial x}\right)|_{\partial D} = 0, \end{aligned} \tag{5}$$

Solving problem (2), (5) one gets:

$$\begin{aligned} \varepsilon_{xx} &= S_{13}\phi_z, \\ \varepsilon_{zz} &= S_{33}\phi_z, \\ \varepsilon_{xz} &= S_{35}\phi_z, \end{aligned} \tag{6}$$

Thus, the second column of the compliance tensor can be recovered.

– z-direction compression:

$$\begin{aligned} \sigma_{xx} &= C_{11}(\omega)\frac{\partial v_x}{\partial x} + C_{13}(\omega)\frac{\partial v_z}{\partial z}|_{x=L_1^x} = 0, \\ \sigma_{xx} &= C_{11}(\omega)\frac{\partial v_x}{\partial x} + C_{13}(\omega)\frac{\partial v_z}{\partial z}|_{x=L_2^x} = 0, \\ \sigma_{zz} &= C_{13}(\omega)\frac{\partial v_x}{\partial x} + C_{11}(\omega)\frac{\partial v_z}{\partial z}|_{z=L_1^z} = 0, \\ \sigma_{zz} &= C_{13}(\omega)\frac{\partial v_x}{\partial x} + C_{11}(\omega)\frac{\partial v_z}{\partial z}|_{z=L_2^z} = 0, \\ \sigma_{xz} &= C_{55}(\omega)\left(\frac{\partial v_x}{\partial z} + \frac{\partial v_z}{\partial x}\right)|_{x=L_1^x} = \psi, \\ \sigma_{xz} &= C_{55}(\omega)\left(\frac{\partial v_x}{\partial z} + \frac{\partial v_z}{\partial x}\right)|_{z=L_1^z} = \psi, \\ \sigma_{xz} &= C_{55}(\omega)\left(\frac{\partial v_x}{\partial z} + \frac{\partial v_z}{\partial x}\right)|_{x=L_2^x} = \psi, \\ \sigma_{xz} &= C_{55}(\omega)\left(\frac{\partial v_x}{\partial z} + \frac{\partial v_z}{\partial x}\right)|_{z=L_2^z} = \psi, \end{aligned} \tag{7}$$

Solving problem (2), (7) one gets:

$$\begin{aligned} \varepsilon_{xx} &= S_{15}\psi, \\ \varepsilon_{zz} &= S_{35}\psi, \\ \varepsilon_{xz} &= S_{55}\psi, \end{aligned} \tag{8}$$

Thus, the third column of the compliance tensor can be recovered.

To construct the effective anisotropic viscoelastic media one needs to solve three boundary value problems for system (1) with with boundary conditions (3), (5), and (7) respectively. After that the strains should be averaged within

the domain D and systems (4), (6), and (8) should be resolved with respect to the components of the compliance tensor. However, to get a unique solution of system (1) we need to add extra no-flow boundary conditions at all boundaries:

$$\vec{w} \cdot \vec{n}|_{\partial D} = 0.$$

To simplify the interpretation of the results it is convenient to consider the seismic wave velocity and attenuation in the effective viscoelastic media [5,23, 26]. To do so, one needs to resolve the dispersion relation for the viscoelastic wave equation. However, the resulting model is anisotropic where the velocity and attenuation depend on the direction of propagation. Thus, we restrict our further considerations with the particular cases; i.e., velocity and attenuation of the quasi-longitudinal or qP-wave propagating along x and z directions and quasi-share or qS-wave propagating along x direction. In 2D orthothropic media qS-wave velocity along x and z directions coincide. We follow [4,23] to estimate the velocities and quality factors:

$$\begin{gathered} V_{px} = \Re\sqrt{\frac{C_{11}}{\rho}},\ V_{pz} = \Re\sqrt{\frac{C_{33}}{\rho}},\ V_s = \Re\sqrt{\frac{C_{55}}{\rho}}, \\ Q_{px} = \frac{\Re C_{11}}{\Im C_{11}}, \quad Q_{pz} = \frac{\Re C_{33}}{\Im C_{33}}, \quad Q_s = \frac{\Re C_{55}}{\Im C_{55}}. \end{gathered} \tag{9}$$

Note that the higher the quality factor the lower the attenuation.

The most time consuming part of the suggested averaging is the numerical solution of equation (1), which is described below.

3 Finite-Difference Approximation

To approximate equation (1) inside the domain $D = [L_1^x, L_2^x] \times [L_1^z, L_2^z]$ we suggest using a regular rectangular grid with steps h_x and h_z. Assume that the domain boundaries have the half-integer coordinates; moreover $L_1^x = x_{1/2}$, $L_2^x = x_{Nx-1/2}$, $L_1^z = z_{1/2}$, $L_2^z = z_{Nz-1/2}$, where N_x and N_z are the numbers of the grid points in corresponding spatial direction. A sketch of the computational domain and the grid is presented in Fig. 3.

We define the grid-functions on a staggered grids so that, u_x and w_x are placed at integer points in x direction, but half-integer points in z direction; whereas u_z and w_z are placed at integer points in z direction, but half-integer points in x direction. That is $(u_x)_{i,j+1/2} = u_x(x_i, z_{j+1/2})$, $(w_x)_{i,j+1/2} = w_x(x_i, z_{j+1/2})$, $(u_z)_{i+1/2,j} = u_x(x_{i+1/2}, z_j)$ and $(w_z)_{i+1/2,j} = w_x(x_{i+1/2}, z_j)$. Thus, the first and the third equations from (1) are approximated in the points $(x_i, z_{j+1/2})$ while the second and the fourth ones are approximated in points $(x_{i+1/2}, z_j)$. All coefficients are stored in half-integer points, assuming that they are constant within the grid cell. To preserve the second order of convergence the share modulus need to be computed at the integer points by the rule [11,15,22,24] (Fig. 1):

$$\frac{1}{\mu_{i,j}} = \frac{1}{\mu_{i-\frac{1}{2},j-\frac{1}{2}}} + \frac{1}{\mu_{i-\frac{1}{2},j+\frac{1}{2}}} + \frac{1}{\mu_{i+\frac{1}{2},j-\frac{1}{2}}} + \frac{1}{\mu_{i+\frac{1}{2},j+\frac{1}{2}}}.$$

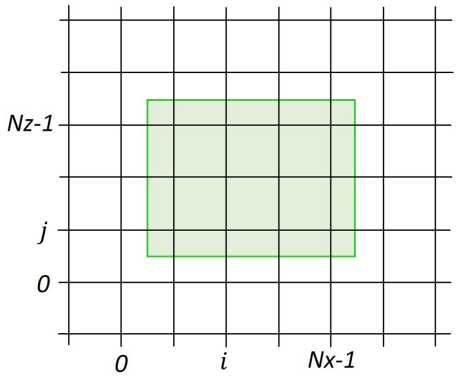

Fig. 1. A sketch of the computational domain and the mesh.

The grid cell and the positions of the solution components are provided in Fig. 2.

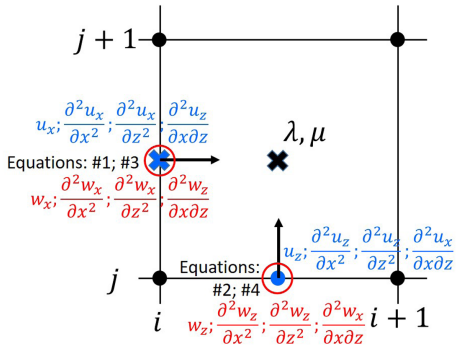

Fig. 2. The grid cell and the positions of the solution components

To approximate equation (1) we use the second order accurate finite differences using the following operators:

$$D_x[f]_{IJ} = \frac{f_{I+1/2,J} - f_{I-1/2,J}}{h_x} = \left.\frac{\partial f}{\partial x}\right|_{x_I, z_J} + O(h_x^2) \tag{10}$$

$$D_z[f]_{IJ} = \frac{f_{I,J+1/2} - f_{I,J-1/2}}{h_z} = \left.\frac{\partial f}{\partial z}\right|_{x_I, z_J} + O(h_z^2) \tag{11}$$

where f is any smooth enough function, and indices I and J can be either integer or half-integer.

Finite-difference approximation of the Eq. (1) produces a system of linear algebraic equations (SLAE) $A_0 x = b$ of the size of $N = 2(N_x-1)N_z+2(N_z-1)N_x$ whose properties are the subject of investigation.

4 Solution of the SLAE

The properties of the constructed system of linear equations should be studied for two different cases. First is nonzero frequency, and the second one is $\omega = 0$; i.e., the static loading.

If the frequency in greater than zero; i.e., $\omega > 0$, the matrix is complex, non-symmetric. Moreover, due to the use of Neumann boundary conditions (3), or (5), or (7) the matrix is singular. The null-space of the differential operator (1), (3) is composed of three vectors:

$$\begin{aligned}(u_x, u_z, w_x, w_z) &= (C_1, 0, 0, 0),\\ (u_x, u_z, w_x, w_z) &= (0, C_2, 0, 0),\\ (u_x, u_z, w_x, w_z) &= (C_3, -C_3, 0, 0),\end{aligned}$$

thus the finite-difference operator has the null-space approximating the presented one.

If the frequency is equal to zero, the right-hand sides of the third and the fourth equations in (1) become trivial. Thus, one may introduce a new variable $V = \nabla \cdot \vec{w} = \frac{\partial w_x}{\partial x} + \frac{\partial w_z}{\partial z}$ and reduces system (1) to

$$\begin{aligned}\frac{\partial}{\partial x}\left[(\lambda_u + 2\mu)\frac{\partial u_x}{\partial x} + \lambda_u \frac{\partial u_z}{\partial z} + \alpha M V\right] + \frac{\partial}{\partial z}\left[\mu\left(\frac{\partial u_x}{\partial z} + \frac{\partial u_z}{\partial x}\right)\right] &= 0,\\ \frac{\partial}{\partial x}\left[\mu\left(\frac{\partial u_x}{\partial z} + \frac{\partial u_z}{\partial x}\right)\right] + \frac{\partial}{\partial z}\left[\lambda_u \frac{\partial u_x}{\partial x} + (\lambda_u + 2\mu)\frac{\partial u_z}{\partial z} + \alpha M V\right] &= 0,\\ \frac{\partial}{\partial x}\left[\alpha M\left(\frac{\partial u_x}{\partial x} + \frac{\partial u_z}{\partial z}\right) + MV\right] &= 0,\\ \frac{\partial}{\partial z}\left[\alpha M\left(\frac{\partial u_x}{\partial x} + \frac{\partial u_z}{\partial z}\right) + MV\right] &= 0,\end{aligned}$$

where only three independent variables present. Thus, the approximation of the derived system will also lead to singular matrix of the rank of $3/4N$.

Therefore matrix A is ill-conditioned for either zero or non-zero frequency ω. We computed the singular value decomposition of matrix A, for small size of the problem ($N \approx 10^4$) and accounted the number of zero singular values to check the null-space dimension.

Solving system of linear equations with singular non-symmetric complex-valued matrix is a challenging task for the iterative methods [20]. Convergence of the iterative solvers is strongly affected by the choice of a preconditioner, which is not the main topic of this research. Moreover, we are dealing with the 2D problems, thus direct methods can be efficiently applied to solve SLAE. In particular, we use the sparse direct solver Intel MKL PARDISO which is very efficiently optimized for Intel architectures.

5 Numerical Experiments

5.1 Homogeneous Media

First we verified the algorithm using a homogeneous model poroelastic model with the following parameters: $\mu = 5.7 \cdot 10^9$ Pa, $\alpha = 0.87$, $\eta = 3 \cdot 10^{-3}$ Pa·s, $\kappa = 10^{-12}$ m^2, $\lambda_0 = 6.09 \cdot 10^9$ Pa, $M = 6.72 \cdot 10^9$ Pa, $\rho = 2650$ kg/m^3, $\rho = 1040$ kg/m^3, $T = 1.5$, and $\varphi = 0.3$. The last four parameters are rock density, fluid density, tortuosity, and porosity respectively. They are not used in quasi-static model, but we need them to estimate the wave propagation velocity and attenuation in the dynamic state.

To simulate the quasi-static loading of the fluid-filled porous material we considered a square domain of the size 1 m, and discretized it by the grid with steps $h_x = h_z = 0.002$ m. Thus the size of the problem was $N_x = N_z = 500$ points. We chose five frequencies $0, 0.1, 1, 10, 100, 1000$ Hz, compute the stiffness tensors and then estimate the velocity and attenuation of the fast P-wave, as presented in Fig. 3. The model was originally homogeneous and isotropic, thus the velocity is independent of the direction of propagation. The only physical factor that causes the attenuation in homogeneous poroelastic media is the Biot flow at high frequencies. However, it can not be resolved in the quasi-static state. Thus, the attenuation of the numerical solution is zero for the entire frequency range. The velocity of the numerical solution is underestimated, but the difference us about 0.1 m/s; i.e. the relative error is $3.5 \cdot 10^{-5}$ which is an acceptable level.

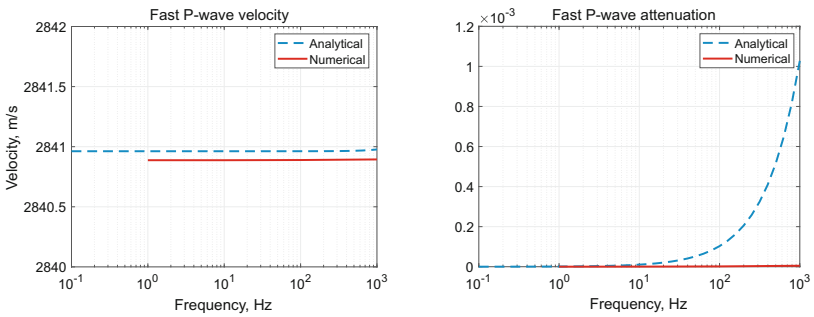

Fig. 3. Comparison of the numerical estimates (red solid line) with analytical solution (blue dashed line). Left picture presents the phase velocity, right picture illustrates the attenuation Q^{-1}. (Color figure online)

5.2 Fractured Media

To illustrate the applicability of the presented approach to estimate the dispersion and dissipation of seismic waves propagating in inhomogeneous poroelastic media, we considered fluid-filled fractured poroelastic model. We used the same

models as those described in [17]. We considered two orthogonal sets of fractures. The fracture length in both sets was fixed to 50 mm and the thickness 2 mm. We generated several types of fractured models, depending on the average percolation length using the simulating annealing technique. Examples of the models are provided in Fig. 4. After that we filled in the model with the material properties. The background was unpermeable, whereas the fracture filling material was relatively hydraulically soft to support the fluid flow. The description of the model is provided in the Table 1. Due to the fracture-to-background wave-induced fluid flows [6,16] local increase of the attenuation, thus velocity dispersion takes place.

Table 1. Material properties.

Parameter	Background	Fracture-filling material
Fluid dynamic viscosity η, Pa·s	0.001	0.001
Permeability k_0, m^2	10^{-15}	$5.5 \cdot 10^{-13}$
Density ρ, kg/m^3	2485	2458
Lame constant λ_u, Pa	$7.159 \cdot 10^9$	$2.40 \cdot 10^{10}$
Shear modulus μ, Pa	$3.0969 \cdot 10^{10}$	$1.14 \cdot 10^{10}$
Biot and Willis constant α	0.2962	0.6078
Fluid storage coefficient M, Pa	$2.01 \cdot 10^{10}$	$9.48 \cdot 10^{10}$

We used the suggested algorithm to estimate the frequency-dependent stiffness tensors for all six model types within the frequency range of $\nu \in [0, ..., 1000]$ Hz. Additionally, we directly simulated wave propagation in fluid-filled fractured-porous media using the approach, described in [17]. Wave propagation was simulated for the Ricker impulse with central frequency 1000 Hz. We provide the velocity and attenuation estimates obtained by the two methods in Figs. 5 and 6 respectively. Note, that the velocities are slightly underestimated by the suggested algorithm, whereas the attenuation matches well. In general, the obtained results show that the increase in the percolation length of the fractured system causes increase in the attenuation due to the FB-WIFF.

5.3 Performance Estimation

In all described examples we used a grid with 500 nodes in both spatial directions. We computed the effective stiffness tensors for the set of 22 frequencies from 0 1000 Hz. A single launch of the algorithm (one model, one frequency) includes the following steps:

1. Approximate problem to get matrix A and right the hand sides b;
2. PARDISO Reordering step. It's a preliminary step to decrease memory consumption and time of the next factorization step.
3. PARDISO Factorization step. It perform LU decomposition of the matrix A.

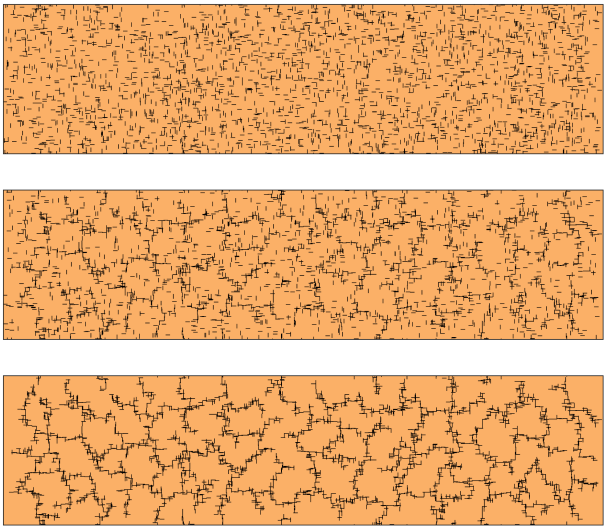

Fig. 4. Models of fractured media with different percolation length (increasing from the top to the bottom).

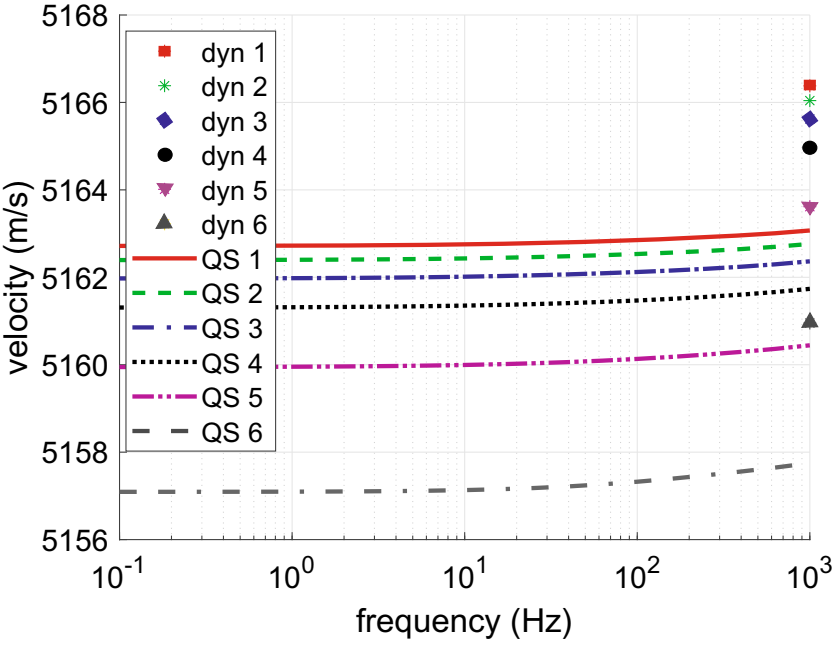

Fig. 5. Velocities of the qP wave for models with different percolation. Lines represent the quasi-static estimates, markers are used for estimates by wave propagation simulation.

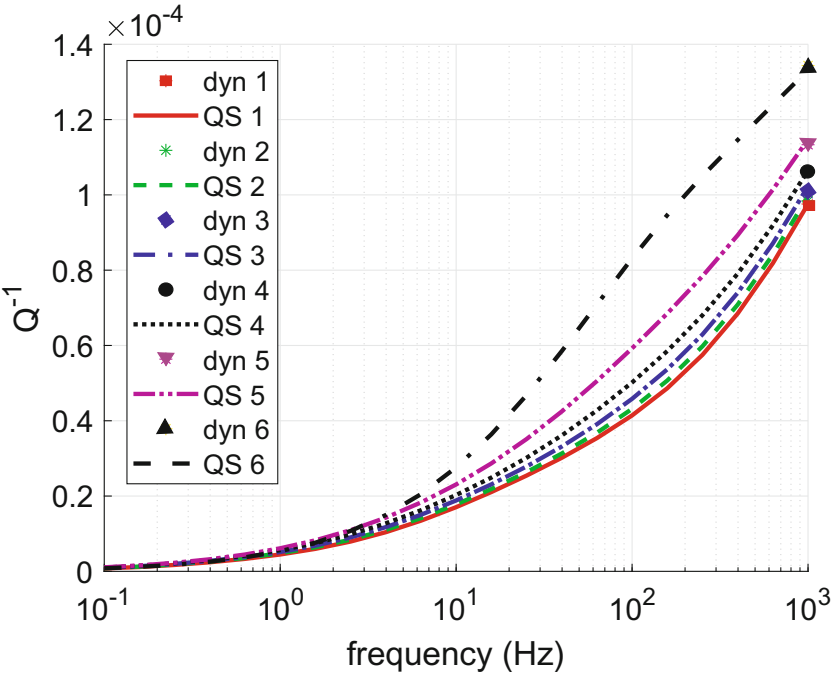

Fig. 6. Attenuation of the qP wave for models with different percolation. Lines represent the quasi-static estimates, markers are used for estimates by wave propagation simulation.

4. PARDISO Solve step. Solve the system to get solution x.
5. Postprocessing: Check the relative residual ($|b - Ax|/|b| \leq 10^{-}12$) and then construct the stiffness tensor C.

Note that if the frequency is changed only the main diagonal of matrix A should be corrected. Thus, step (1) can be done for zero-frequency but only the diagonal entries are changed at further loops of the algorithm. The reordering step (2) depends just on position non-zero elements A and can be done only once but applied for all ω. As a result, the entire algorithm (steps 1–5) is applied only to the first frequency in the raw, whereas the reduced version of the algorithm (steps 3–5) can be applied to all other frequencies.

We used Intel(R) Xeon(R) CPU E5-2690 v2 @ 3.00 GHz with 20 cores in our simulations. The computational time for one model and all 22 frequencies is ≈ 140 s. The timing profiling of the 22 runs is:

1. Approximate problem: ≈ 3 s.
2. PARDISO Reordering step: ≈ 4 s.
3. PARDISO Factorization step. $22 \times (\approx 3 - 4$ s.)
4. PARDISO Solve step. $22 \times (\approx 0.8$ s.)
5. Postprocessing: $22 \times (\approx 0.4$ s.)

Execution of the algorithm for the problem size of 500^2 required about 8 Gb RAM, thus it can be done on any desktop machine, or ported to a standard GP-GPU to improve performance.

6 Conclusions

We presented a numerical algorithm to simulate low-frequency loading of fluid-filled poroelastic materials and estimate the effective frequency-dependent strain-stress relations for such media. The algorithm solves Biot equation in quasi-static state. The problem is parabolic, thus, it is convenient to solve it in the frequency domain. As a result a system of linear algebraic equations have to be solved for each temporal frequency. We use the direct solver, based on the *LU* decomposition to resolve the SLAE. According to the presented numerical examples the suggested algorithm allows reconstructing the stiffness tensor within a wide range of frequencies $[0, ..., 1000]$ Hz, for the realistic sample size within 2–3 min. Thus, it allows to perform series of numerical experiments using simulations as the part of topological optimization techniques. Note, that our implementation is oriented on the use of CPU, whereas porting the algorithm to GPU would further improve the performance.

References

1. Bazaikin, Y., et al.: Effect of CT image size and resolution on the accuracy of rock property estimates. J. Geophys. Res. Solid Earth **122**(5), 3635–3647 (2017)
2. Biot, M.A.: Theory of propagation of elastic waves in a fluid-saturated porous solid. ii. higher frequency range. J. Acoust. Soc. Am. **28**, 179–191 (1956)
3. Biot, M.A.: Theory of propagation of elastic waves in fluid-saturated porous solid. i. low-frequency range. J. Acoust. Soc. Am. **28**, 168–178 (1956)
4. Carcione, J.M., Cavallini, F.: A rheological model for anelastic anisotropic media with applications to seismic wave propagation. Geophys. J. Int. **119**, 338–348 (1994)
5. Christensen, R.M.: Theory of Viscoelasticity, an Introduction. Academic Press, New York (1971)
6. Germán Rubino, J., Guarracino, L., Müller, T.M., Holliger, K.: Do seismic waves sense fracture connectivity? Geophys. Res. Lett. **40**(4), 692–696 (2013)
7. Guo, J., Rubino, J.G., Glubokovskikh, S., Gurevich, B.: Effects of fracture intersections on seismic dispersion: theoretical predictions versus numerical simulations. Geophys. Prospect. **65**(5), 1264–1276 (2017)
8. Huang, F., et al.: The first post-injection seismic monitor survey at the Ketzin pilot CO2 storage site: results from time-lapse analysis. Geophys. Prospect. **66**(1), 62–84 (2018)
9. Hunziker, J., et al.: Seismic attenuation and stiffness modulus dispersion in porous rocks containing stochastic fracture networks. J. Geophys. Res. Solid Earth **123**(1), 125–143 (2018)
10. Kong, L., Gurevich, B., Zhang, Y., Wang, Y.: Effect of fracture fill on frequency-dependent anisotropy of fractured porous rocks. Geophys. Prospect. **65**(6), 1649–1661 (2017)

11. Lisitsa, V., Podgornova, O., Tcheverda, V.: On the interface error analysis for finite difference wave simulation. Comput. Geosci. **14**(4), 769–778 (2010)
12. Marty, N.C.M., Hamm, V., Castillo, C., Thiéry, D., Kervévan, C.: Modelling water-rock interactions due to long-term cooled-brine reinjection in the Dogger carbonate aquifer (Paris basin) based on in-situ geothermal well data. Geothermics **88**, 101899 (2020)
13. Masson, Y.J., Pride, S.R., Nihei, K.T.: Finite difference modeling of Biot's poroelastic equations at seismic frequencies. J. Geophys. Res. Solid Earth **111**(B10), 305 (2006)
14. Menke, H.P., Reynolds, C.A., Andrew, M.G., Pereira Nunes, J.P., Bijeljic, B., Blunt, M.J.: 4D multi-scale imaging of reactive flow in carbonates: assessing the impact of heterogeneity on dissolution regimes using streamlines at multiple length scales. Chem. Geol. **481**, 27–37 (2018)
15. Moczo, P., Kristek, J., Vavrycuk, V., Archuleta, R.J., Halada, L.: 3D heterogeneous staggered-grid finite-difference modeling of seismic motion with volume harmonic and arithmetic averaging of elastic moduli and densities. Bull. Seismol. Soc. Am. **92**(8), 3042–3066 (2002)
16. Muller, T.M., Gurevich, B., Lebedev, M.: Seismic wave attenuation and dispersion resulting from wave-induced flow in porous rocks – a review. Geophysics **75**(5), 75A147-75A164 (2010)
17. Novikov, M.A., Lisitsa, V.V., Bazaikin, Y.V.: Wave propagation in fractured-porous media with different percolation length of fracture systems. Lobachevskii J. Math. **41**(8), 1533–1544 (2020)
18. Ovaysi, S., Wheeler, M., Balhoff, M.: Quantifying the representative size in porous media. Transp. Porous Media **104**(2), 349–362 (2014)
19. Rubino, J.G., Muller, T.M., Guarracino, L., Milani, M., Holliger, K.: Seismoacoustic signatures of fracture connectivity. J. Geophys. Res. Solid Earth **119**(3), 2252–2271 (2014)
20. Saad, Y.: Iterative Methods for Sparse Linear Systems. SIAM (2003)
21. Salaun, N., et al.: High-resolution 3D seismic imaging and refined velocity model building improve the image of a deep geothermal reservoir in the Upper Rhine Graben. Lead. Edge **39**(12), 857–863 (2020)
22. Samarskii, A.A.: The Theory of Difference Schemes, Pure and Applied Mathematics, vol. 240. CRC Press (2001)
23. Vavrycuk, V.: Velocity, attenuation, and quality factor in anisotropic viscoelastic media: a perturbation approach. Geophysics **73**(5), D63–D73 (2008)
24. Vishnevsky, D., Lisitsa, V., Tcheverda, V., Reshetova, G.: Numerical study of the interface errors of finite-difference simulations of seismic waves. Geophysics **79**(4), T219–T232 (2014)
25. Xu, C., Dowd, P.A., Mardia, K.V., Fowell, R.J.: A connectivity index for discrete fracture networks. Math. Geol. **38**(5), 611–634 (2006)
26. Zhu, Y., Tsvankin, I.: Plane-wave propagation in attenuative transversely isotropic media. Geophysics **71**(2), T17–T30 (2006)